Research Article | Vol. 28, No. 5 / 2 March 2020 / Optics Express 6277
Optics EXPRESS

Automatic fringe pattern enhancement using truly adaptive period-guided bidimensional empirical mode decomposition

PAWEŁ GOCŁOWSKI,[1] MACIEJ TRUSIAK,[1,*] AZEEM AHMAD,[2] ADAM STYK,[1] VICENTE MICO,[3] BALPREET S. AHLUWALIA,[2] AND KRZYSZTOF PATORSKI[1]

[1]*Warsaw University of Technology, Institute of Micromechanics and Photonics, 8 Sw. A. Boboli St., 02-525 Warsaw, Poland*
[2]*Department of Physics and Technology, UiT The Arctic University of Norway, NO-9037 Tromsø, Norway*
[3]*Universitat de Valencia, Departamento de Óptica y Optometría y Ciencias de la Visión, Burjassot, Spain*
[*]*maciej.trusiak@pw.edu.pl*

Abstract: Fringe patterns encode the information about the result of a measurement performed via widely used optical full-field testing methods, e.g., interferometry, digital holographic microscopy, moiré techniques, structured illumination etc. Affected by the optical setup, changing environment and the sample itself fringe patterns are often corrupted with substantial noise, strong and uneven background illumination and exhibit low contrast. Fringe pattern enhancement, i.e., noise minimization and background term removal, at the pre-processing stage prior to the phase map calculation (for the measurement result decoding) is therefore essential to minimize the jeopardizing effect the mentioned error sources have on the optical measurement outcome. In this contribution we propose an automatic, robust and highly effective fringe pattern enhancement method based on the novel period-guided bidimensional empirical mode decomposition algorithm (PG-BEMD). The spatial distribution of the fringe period is estimated using the novel windowed approach and then serves as an indicator for the truly adaptive decomposition with the filter size locally adjusted to the fringe pattern density. In this way the fringe term is successfully extracted in a single (first) decomposition component alleviating the cumbersome mode mixing phenomenon and greatly simplifying the automatic signal reconstruction. Hence, the fringe term is dissected without the need for modes selection nor summation. The noise removal robustness is ensured employing the block matching 3D filtering of the fringe pattern prior to its decomposition. Performance validation against previously reported modified empirical mode decomposition techniques is provided using numerical simulations and experimental data verifying the versatility and effectiveness of the proposed approach.

1. Introduction

Fringe analysis is a central aspect of many contemporary full-field optical measurement techniques, i.e., interferometry, fringe projection and quantitative phase imaging, crucial in nowadays technical and biomedical non-contact investigations. Final accuracy of the optical measurement substantially depends on the algorithmic solution used to extract the phase map from the recorded intensity distribution [1–4]. Phase, determined by the local shape, period and position of fringes, stores the information about the object/phenomenon under study. Under out-of-laboratory data acquisition conditions it is difficult to make use of the temporal phase shifting [1–4] method providing the highest accuracy. Stringent requirements on the recording of the component interferograms complicate the process of the data acquisition and analysis. Single-shot approaches are much more immune to the environmental disturbances and require generally simpler experimental setups. Additionally, they enable investigating transient events. Their accuracy and scope

#382543 https://doi.org/10.1364/OE.382543
Journal © 2020 Received 12 Nov 2019; revised 23 Jan 2020; accepted 24 Jan 2020; published 19 Feb 2020

Optics EXPRESS

depends mainly on the algorithmic solutions applied as in the real life experiments, mainly in experimental mechanics, material testing, quantitative bio-phase imaging applications, a single fringe pattern contains noise, non-uniform background and intensity modulation variations.

Among dynamically developed single frame automatic fringe pattern analysis techniques one can highlight: Fourier transform [5], windowed Fourier transform [6–7], continuous wavelet transform [8–11], regularized phase tracking [12–15], spatial carrier phase shifting [16–18], Hilbert spiral transform (HST) [19], monogenic signal based approach [20], implicit smoothing splines [21] and digital signal estimation methods [22–24]. The most versatile and efficient solutions have very high computational load, parameter-dependence and rather long processing time [6–24]. Practical challenges include appropriate carrier fringe applications [5–18], error propagation [5,12–18, 21–24], susceptibility to noise, fringe modulation/background/period local significant variations [5–24], and locally closed concentric fringes [5–20,22–24]. Particular case of single-shot analysis of closed or significantly bent fringes (with substantial orientation and period local variations) is encountered very often where there is no setup solution for the full carrier fringe implementation or it is not introduced for the sake of accuracy and bandwidth optimization (and the phenomena under study are too fast for phase-shifting). Moreover, using high NA objectives for studying detailed micro-objects in digital holographic microscopy one often encounters the overlapping of the cross-correlation and the auto-correlation terms in Fourier spectrum. Classical approaches with the Fourier/wavelet transforms (in general integral quadrature transformations for the analytic signal generation) often fail to demodulate the phase due to the overlapped spectrum, sign ambiguity and high local phase gradients [5–11,16–18]. These central obstacles can be overthrown, e.g., by appropriately performed HST [18], regularized phase tracking [12–15] and intrinsic smoothing splines [21]. These families of effective fringe demodulation techniques do need the fringe pattern pre-processing, however. Efficient fringe pattern background filtering (essential in all techniques), noise minimization and contrast normalization (vital in regularized phase tracking) [25,26] play therefore a pivotal role in the single-shot optical full field measurement. Among contemporary filtering techniques the empirical mode decomposition (EMD) stands out as a vividly blossoming method with constantly increasing number of applications. Interestingly, integral transformation based single-frame fringe pattern analysis methods can also benefit from the EMD-related pre-filtering procedure (i.e., solutions presented for enhancing Fourier transform [27,28], Windowed Fourier transform [29] and continuous wavelet transform [30]).

The original one-dimensional EMD was firstly proposed by Huang et al. in [31] as an adaptive and data-driven approach for nonlinear and nonstationary data analysis. Oppositely to the Fourier methods, no predefined decomposition basis is used; it is determined by the signal itself (its extrema distribution to be precise). The bidimensional EMD (BEMD) is a fully two-dimensional method, which interpolates envelope surfaces of the corresponding image extrema with functions as bidimensional cubic splines [32] or radial based functions [33]. Some comparison of the different interpolation techniques is given in [34]. Reported applications of the BEMD in the fringe pattern processing and analysis considered the noise reduction in digital speckle interferometry [35], fringe pattern background removal [36,27] and normalization [37], phase measurement [38] and amplitude demodulation [39]. The practical impact of the BEMD was severely limited by the calculation time – the spline interpolation on the irregular grid is the most expensive part of the algorithm. It was even more of an issue in 2D ensemble EMD [40,41], technique for the noise-assisted data analysis with increased efficiency of the signal component separation. To overcome this limitation Fast Adaptive BEMD (FABEMD) approach was proposed by Bhuiyan et al. [42]. The envelope generation is modified by replacing the 2D surface interpolation by an order-statistics-based filtering followed by a smoothing operation. Each mode is extracted using the different (increasing) filtering sliding-window width which resulted in ensuring basic level of adaptivity. Besides significantly shortening the computation time, more

Optics EXPRESS

accurate estimation of the bidimensional intrinsic mode functions (BIMFs), representing image features at various spatial scales, is to be obtained in many cases. The FABEMD algorithm was employed in the fringe analysis [43], moiré techniques [44,45], grating interferometry [46] and image fusion [47]. The enhanced and fast EMD algorithm (EFEMD) proposed in 2014 [48] provided further acceleration with preserved high quality of the resulting set of BIMFs. The filtering window size is quickly estimated using the number of extrema, not the distance between the adjacent ones (like in the FABEMD), and the morphological dilation is employed to speed up the envelope estimation and extrema detection steps. With the decomposition time reduced to as much as a fraction of a second new possibilities opened up and resulted in EFEMD applications in fringe analysis [48–50], two-frame interferometry [51,52], three-beam interferometry [53], and biomedical imaging using structured illumination microscopy [54], quantitative phase imaging [55] and interference phase microscopy [56], to name some.

Although significant enhancement was incorporated into the BEMD concept, it still suffers from the mode mixing phenomenon defined as the information spreading over several modes or mixing in a single one. The mode mixing, especially visible in the FABEMD/EFEMD techniques providing rather high number of modes, is limiting the fringe pattern filtering ability in terms of the cumbersome decision making system upon fringe part reconstruction (addition of selected modes) and the increased risk of the information loss and noise transfer. It is therefore highly desirable to avoid the mode mixing, e.g., using the sinusoid assisted decomposition [57] or employing the automatic selective reconstruction scheme [48], and/or concentrate the fringe part in a single mode, e.g., modifying the envelope construction part [58]. In this contribution we present a novel technique named the period-guided bidimensional empirical mode decomposition (PG-BEMD), able to extract a complete fringe component condensed in the first mode using the local fringe density map guidance. The PG-BEMD is carefully described with relation to its predecessors in Section 2. Section 3 contains numerical verification in comparison with the EFEMD algorithm [48] and the reference method for the sparse decomposition – the morphological operation based BEMD (MO-BEMD) [58]. Section 4 comprises experimental validation. It is worth showcasing that variational image decomposition techniques, recently flourishing in the fringe analysis [59,60], operate on a notion of sparsely extracting single fringe component. Nevertheless they stay out of the scope of this study due to significantly distinctive *modus operandi* of the decomposition based on the total variation approach and the iterative projection algorithm.

2. The PG-BEMD technique description

2.1. Working principle of the PG-BEMD and selected reference methods

The PG-BEMD algorithm is presented here as a significant advancement of the previously reported EFEMD algorithm, established on the notion of FABEMD and BEMD. It was combined with the automatic selective reconstruction scheme to minimize the mode mixing utilizing only selected high contrast areas of each informative mode. The EFEMD algorithm operates estimating upper and lower envelopes with morphological disk-shaped filters of the diameter d determined by the number of detected extrema. First mode is generated subtracting the mean envelope from the initial image, next modes are extracted iteratively analyzing in a similar way the subsequent mean envelopes. For the full decomposition this loop continues until the mean envelope is close enough to the monotonous signal, i.e., contains highly limited number of extrema. Implementation based on morphological operations is very efficient and allowed significant reduction of the computation time. It is not fully adaptive, however. Determined filtering kernel size (diameter d) is spatially constant for the extraction of a given mode, regardless the local shape of the fringes (the local distribution of extrema). It results in the amplified mode mixing effect which is considered as a pejorative feature. In the presented PG-BEMD approach we propose to use the sliding-window filtering and spatially vary the width of the squared window adjusting it to the local fringe pattern

Optics EXPRESS

density. Expected outcome comprises concentration of all the essential fringe information in a single decomposition component (first mode). Consequently, mode mixing phenomenon is to be completely omitted and fringe reconstruction becomes automatic and straightforward (no need for any modes selection). In the next subsections we will discuss the efficient implementation of proposed novel method. The PG-BEMD will be briefly compared with the already described original EFEMD algorithm and evaluated using the mode-mixing-reduced MO-BEMD method [58] (state-of-the-art approach in sparse BEMD).

In preparation for the numerical analysis we introduce the selected reference decomposition technique. The MO-BEMD was proposed in [58] for the efficient fringe pattern background term elimination. The sparse decomposition into three components, namely the noise part, fringe term and background, was achieved determining the local filter size basing on the pixel distance from the nearest ridge/trough, as the idea of interpolation nodes is significantly different here. The MO-BEMD employs the morphological top hat transform to detect ridges and troughs of the fringes, and uses the weighted moving average algorithm to estimate the envelopes, replacing the respective local extrema detection and the envelope interpolation of conventional BEMDs. The initial ridge/trough map is to be refined due to noise, varying period and contrast related problems. Next the Euclidean distance transform is calculated; subsequently it guides the coarse and smoothed envelope estimation. The background intensity of the fringe pattern is automatically removed by extracting the single mode in an iterative process, thereby addressing the mode mixing problem. The top-hat transform based fringe skeletoning, which is susceptible to the fringe shape fluctuations and noise, limits the MO-BEMD to rather continuous and clearly visible low-to-medium density fringe patterns. Strong sample-induced fringe quality deteriorations commonly encountered, e.g., in quantitative phase imaging (QPI) and digital holographic microscopy [55,56,61–63] can be therefore problematic. On the contrary, the proposed PG-BEMD is designed to support QPI in its emerging development to become a versatile optical imaging tool for biomedical study.

Starting from the next subsection we will quantitatively evaluate developed advancements of the PG-BEMD in terms of the root mean squared (RMS) error calculation. The RMS is defined as the variance of the difference between the first decomposed mode and the cosine of the ideal phase. The latter is seen as the reference fringe pattern – the simulated ideal phase function is accessible in numerical testing. The first mode is expected to be very similar to the cosine of the phase for increasing the decomposition quality.

2.2. PG-BEMD: boundary aware fringe pattern envelope estimation

The FABEMD/EFEMD algorithms exhibit generally good behavior at the image borders, which was particularly troublesome with the triangulation-based BEMD methods [32–41]. The envelope estimation employing the default Matlab functions (imdilate and conv2) utilize the Fourier transform and go beyond the image boundaries referring to the non-existent pixels, however the mirror extension of the image in its preprocessing is therefore employed. In some cases it can introduce awkward local intensity distribution leading to edge artifacts. Exemplifying simulated fringe pattern after mirroring procedure is presented in Fig. 1(a), whereas second mode of the classical EFEMD decomposition in shown in Fig. 1(b). Edge artifacts, i.e., distortion of fringes, can be clearly observed in Fig. 1(b). They influence the overall quality of the fringe pattern filtering, therefore a method for their reduction is desirable. In this virtue we employ dilation and averaging functions based on the boundary-aware shape-adjusted direct pixel's neighbourhood instead of the Fourier Transform. Highest value from the pixel neighbourhood is set as the filtered pixel value in the dilation operation. Similarly, the arithmetic average of values from the neighbourhood is set as the filtered pixel value in averaging operations. Neighbourhood functions contain image domain boundary aware [64] conditions removing the necessity of the

Optics EXPRESS

extrapolation. Edge errors minimization can be observed in Fig. 1(c), in comparison with Fig. 1(b).

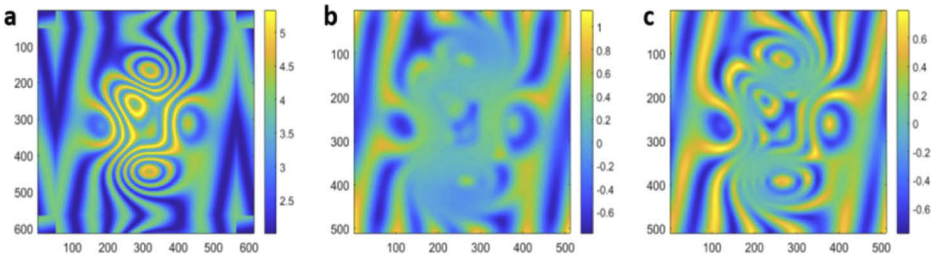

Fig. 1. (a) Simulated fringe pattern after mirroring procedure, (b) its 2nd mode containing edge errors and (c) 2nd mode after edge errors removal.

2.3. *PG-BEMD: novel adaptive windowed approach for local fringe pattern density estimation*

In the EFEMD algorithm the fringe component with phase information is stored in a several different modes. Merging some of them together to reconstruct the complete fringe term is a time-consuming and cumbersome task (there is a risk of losing information and noise transfer). We propose the decomposition with spatially adaptive filter size as an original solution of the mode-mixing problem. The working principle encompasses applying small filter size in dense fringe areas and large filters in sparse fringe areas. This novel approach requires the local fringe density map estimation to guide the spatially adaptive decomposition. Local fringe density map, understood as the local fringe spatial frequency and period estimate, is one of the main parameters in the fringe pattern analysis [65] and was explored in single frame phase demodulation using the modified regularized phase tracking [13], windowed Fourier transform [66] and sequential techniques [67–69]. Initially, we computed the fringe density map based on the orthogonal spatial derivatives of the phase. By definition, fringe density, or more precisely spatial frequency, is computed as the modulus of the gradient of the underlying phase function (which is accessible in numerical simulations). Utilizing the 'ideal' density map we primarily verified the ability to contain complete fringe information in single first mode. Naturally, access to the phase map is not granted in the experimental reality; to circumvent this limitation we proposed the novel original fringe density map estimator. We use the simulated fringe pattern, Fig. 2(a), to clearly explain the local filter size determination scheme based on the fringe density map estimation procedure. It is a central aspect of the novel PG-BEMD algorithm. Note red and orange spots in Fig. 2(a) indicating exemplifying pixel locations of denser and sparser fringes, respectively.

Fringe pattern shown in Fig. 2(a) was simulated using the following Matlab code:

```
[x y]=meshgrid(linspace(-pi,pi,512));
phase=x.^3/5 - 11*x - 2*y.^2+10*y+6*peaks(512);
gauss=10*normpdf(x.^2+y.^2,0,3); Im=3+cos(phase)+gauss;
```

where *phase* denotes the equation describing the phase of the interferogram, *gauss* is the Gaussian background on the fringe pattern, *Im* is the final fringe pattern.

Our novel original fringe density map estimator works in a pixel-by-pixel manner and contains the following steps (for a given selected pixel, we start with red location):

a) The algorithm computes the arithmetic average from the smallest (3×3) pixel's neighbourhood, see the yellow area in Fig. 2(b). The currently analysed pixel is marked with a red square in Fig. 2(a). In this case the neighbourhood average equals 3,11.

Optics EXPRESS

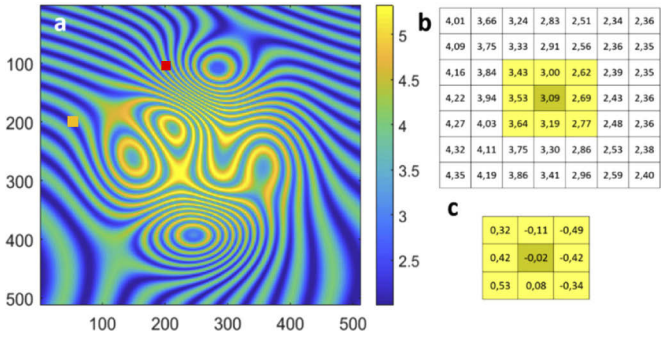

Fig. 2. (a) Simulated fringe pattern, (b) selected pixel's neighbourhood, (c) selected pixel neighbourhood with differences between intensity values and arithmetic average.

b) For every pixel in the neighbourhood the difference between the average (3,11) and the pixel's value is computed, see Fig. 2(c).

c) The average of the absolute values of these differences is computed, here it equals 0,303.

d) The algorithm checks if this average difference is larger than the limit value. It is set as $0{,}1(I_{max}\text{-}I_{min})$, where I_{max} is the highest intensity and I_{min} is the lowest intensity in the image. Value of 0,1 is recommended after investigating the RMS dependence on b, where the limit value equals $b(I_{max}\text{-}I_{min})$, see plot Fig. 3. The RMS was calculated comparing the ideal fringe term with the first mode extracted using the PG-BEMD. For fringe pattern presented in Fig. 2, I_{max} equals 5,33 and I_{min} equals 2, thus limit value is 0,333.

e) If average difference is larger than the limit value, current neighbourhood size is saved as the local density. If not, points a)-d) are repeated with consequently increasing neighbourhoods (5×5, 7×7 etc.) until this condition is fulfilled. At the end, the local density is multiplied by 2 and used as a local decomposition filter size for subsequent dilation and averaging. We recommend multiplying by 2 after investigating the RMS dependence on the multiplication value (parameter a), see Fig. 4. As limit value has not been achieved ($0{,}303 < 0{,}333$), the operation is to be repeated with 5×5 neighbourhood. This time the average difference equals 0,492. The limit value has been achieved, so 5×5 neighbourhood was multiplied by 2 and the value of 10 has been assigned as a local filter width. In fact, small neighbourhood containing one fringe or less will not achieve the limit value, unlike the bigger one, containing a few fringes. The algorithm is very sensitive to the steep fringe slope. Usually, after achieving the limit the mask size does not cover completely the fringe period, rather encompasses its halve, which is precisely why *a posteriori* 2x multiplication is needed.

We have repeated all the operations for another pixel in the area with sparse fringes (marked with orange spot in Fig. 2(a)). As established, we started with the smallest neighbourhood, 3×3 pixels. The average deviation has not achieved the limit value (0,333) until 19×19 pixels neighbourhood. All average deviations are listed in Table 1 indicating almost linear increase until reaching the predefined limit (PG-BEMD threshold). Described method allowed us to get the complete fringe density map (Fig. 5(a)) without any *a priori* knowledge. In comparison, the simulated phase-derivative-based map is shown at Fig. 5(b), after rescaling to the filter size.

The PG-BEMD decomposition results of the simulated exemplifying interferogram (showed in Fig. 2(a)) are presented in Fig. 6. Proposed original solution in terms of the local adjustment of the filter size guided by the fringe period estimator allowed us to contain complete fringe information in the single first mode, see Fig. 6(a). The rest of the decomposition components, BIMFs no.

Optics EXPRESS

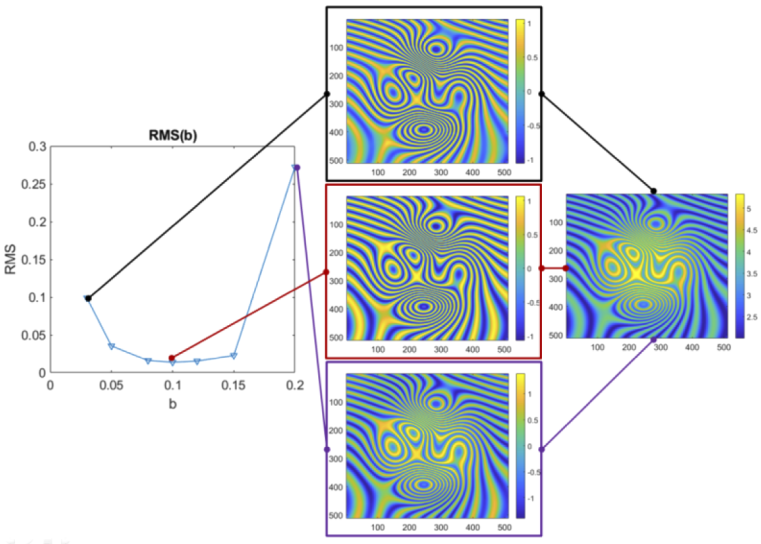

Fig. 3. Studying the threshold value for the fringe density estimator: plot indicating the RMS values calculated for the first extracted mode using the PG-BEMD method with varying the b parameter determining the averaged intensity limit, i.e., $b(I_{max}\text{-}I_{min})$. Simulated initial fringe pattern is depicted on the right hand side.

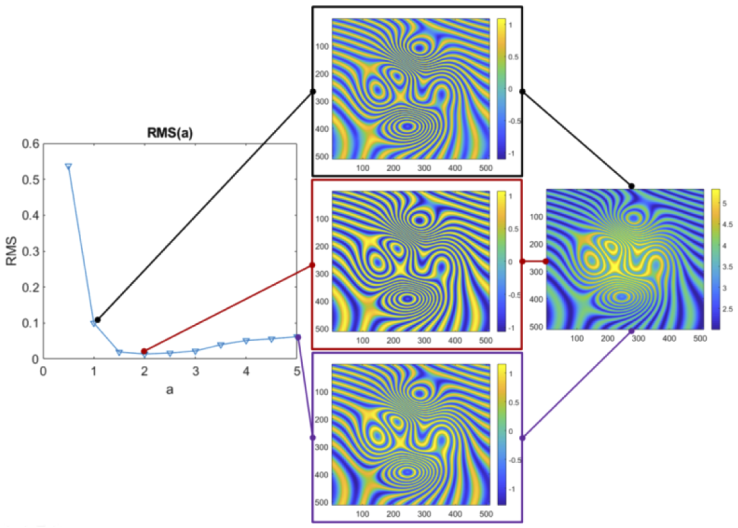

Fig. 4. Studying the multiplication parameter a value for the local PG-BEMD filter size determination: plot indicating the RMS values calculated for the first extracted mode using the PG-BEMD method with the b parameter set to 0,1 and the a parameter varying. Simulated initial fringe pattern is depicted on the right hand side.

Table 1. Averaged deviation values calculated for increasing neighborhoods in sparse fringe region (orange dot in Fig. 2(a)).

Neighb. size	3 × 3	5 × 5	7 × 7	9 × 9	11 × 11	13 × 13	15 × 15	17 × 17	19 × 19
AvDeviation	0,017	0,037	0,066	0,103	0,148	0,196	0,249	0,304	0,356

Optics EXPRESS

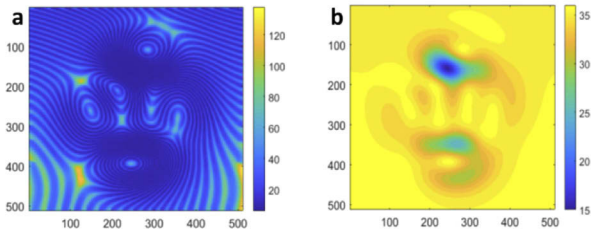

Fig. 5. (a) A pixel-by-pixel neighbourhood-based fringe density map estimate and (b) the reference phase-derivative-based fringe density map estimate.

2, 3 and 4 (presented in Figs. 6(b), 6(c) and 6(d), respectively), constitute residual information connected with the low frequency background term. In further analysis we will skip these modes, as they do not provide any important fringe information. First mode will be automatically treated as the final filtering result. We compared our novel PG-BEMD decomposition result to the 'ideal' cosine of the phase, Fig. 6(e), and to the first mode obtained guiding the decomposition by the phase-derivative-based density map, Fig. 6(f). For complete comparison Fig. 7 shows the EFEMD results.

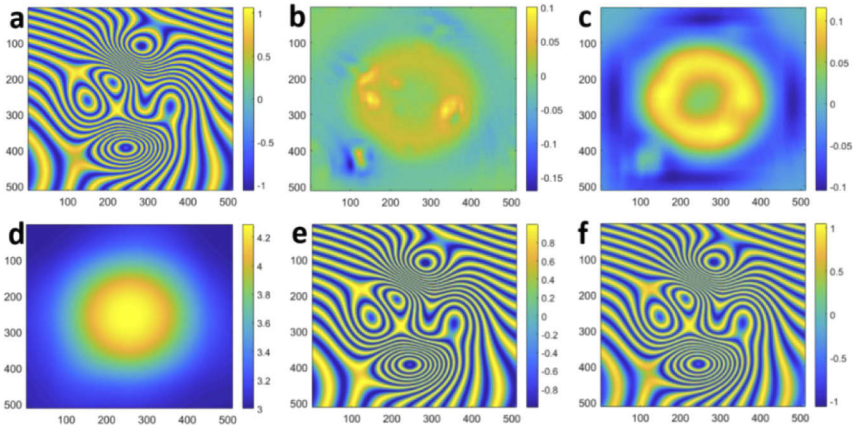

Fig. 6. The complete PG-BEMD decomposition results: (a) 1st mode, (b) 2nd mode, (c) 3rd mode and (d) 4th mode; (e) the cosine of the ideal phase and (f) the first mode from decomposition using phase-derivative-based fringe density map.

We also computed three RMS values after decomposition:

The EFEMD (Fig. 7(d)) RMS: 0,074,

The phase-derivative-based density map (Fig. 6(f)) RMS: 0,049,

The PG-BEMD (Fig. 6(e)) RMS: 0,022.

The PG-BEMD algorithm compares favourably with the EFEMD and the phase-derivative based approaches. In the EFEMD algorithm the phase information (the fringe component) is stored in the first 3 modes and its further reconstruction is needed. Even after merging first 3 modes into one image its RMS is still much higher than in the PG-BEMD algorithm. What is more, there is often a necessity of time consuming selective reconstruction (e.g., mode contains sharply extracted locally dense fringes and part of background). In theory, the decomposition using the phase-derivative-based (ideal) density map should be the best. We were using linear scaling of

Optics EXPRESS

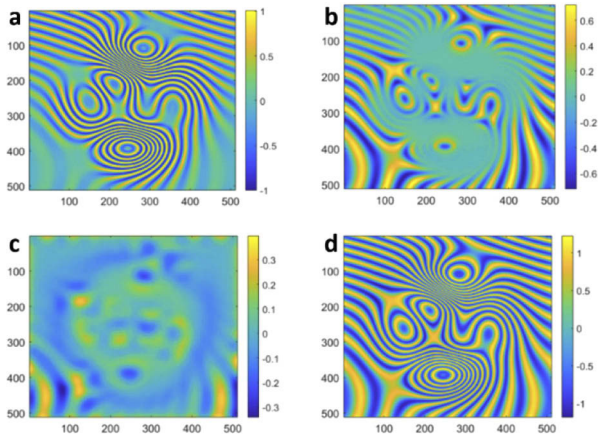

Fig. 7. The EFEMD decomposition results: (a), 1st mode (b), 2nd mode (c), 3rd mode (d) and sum of first 3 modes.

the phase gradient value to the fringe density map – it may not be optimal. However, further study of the phase-derivative-based density map is out of the scope of this paper as it already served the introduction and comparison purpose very well.

3. Numerical evaluation using synthetic fringe patterns

In this section we will test and verify the proposed PG-BEMD algorithm by studying its various features using simulated interferograms. In numerical examination we can precisely design the testing conditions to comprehensively evaluate the novel decomposition method. We also do have an ideal reference interferogram, in terms of the cosine function of the simulated phase, which enables quantitative appraisal of the PG-BEMD method. We will focus on the influence of the noise, carrier spatial frequency and the background term on the PG-BEMD performance in comparison with the MO-BEMD reference algorithm.

3.1. The BM3D-based solution to the noise transferring problem

As shown in Section 2 the proposed novel PG-BEMD algorithm can be seen as a great tool for the zero-mean-value fringe term dissection, perfectly suited for subsequent Hilbert transform analysis. Background illumination component (incoherent sum of intensities of two interfering beams in classical two beam interferometry) and other low spatial frequency terms are effectively removed in automated and decision-free manner. Unfortunately, at this stage no high spatial frequency filter is included and practically all noise is transferred to the first mode, see Fig. 8. It is worth to note, however, that noise is not influencing the density map estimator as complete fringe component is still dissected in the first mode, Fig. 8(b).

The noise transferring problem reduces the PG-BEMD algorithm's usefulness in the real interferogram analysis. It is therefore desirable to conduct the denoising prior to the PG-BEMD decomposition to increase its quality and robustness to the noise. In the MO-BEMD method, previously reported state-of-the-art sparse empirical decomposition, the block matching 3D collaborative filtering (BM3D) algorithm [70] was employed for the denoising. It had default settings on, however. Recently we performed an in-depth study on the sigma-tailored BM3D denoising for the fringe pattern analysis [60]. Sigma is the most important BM3D parameter as it estimates the Gaussian noise level present in the image and steers the BM3D denoising. Studies shown that the sigma value can be significantly increased from the default 20 due to local and

Optics EXPRESS

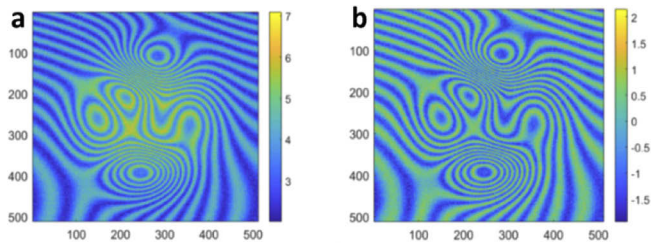

Fig. 8. (a) Input image with noise added and (b) its first mode calculated using the proposed PG-BEMD method (note successfull background removal and no denoising).

non-local self-similarity of the fringe pattern physically determined by the interference-based quasi-periodic sinusoidal term. For exemplifying sigma value (=60) we present, in Fig. 9, plot illustrating the relation between the regular PG-BEMD and BM3D enhanced PG-BEMD for a wide range of the noise values (variances of added Gaussian noise). Presented plot showcases a tremendous and stable reduction of the noise influence using the BM3D which is beneficial for all variances bigger than 0,1. Very low noise and ideal zero noise scenarios are out of the scope of the BM3D algorithm, however. In these cases informative components are partially eliminated upon denoising due to lack of the noise itself. It suggests to use lower sigma (5-10) in the cases of the detail-rich biological object study, like in QPI [61–63] or fluorescent microscopy [71].

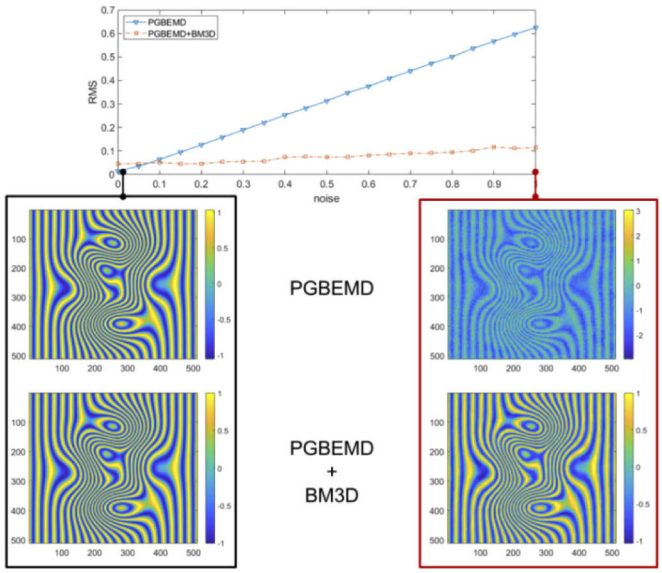

Fig. 9. The PG-BEMD and PG-BEMD + BM3D comparison, according to varying noise. Y axis contains RMS error values, X axis presents variance of added white Gaussian noise.

3.2. *Fringe pattern feature investigation – carrier spatial frequency*

Using the previously described Matlab codes and altering the phase formula:

```
phase = B*x + 3*peaks(512);
```

we simulated a set of fringe patterns with varying carrier spatial frequency (parameter B). The objective of this study is to test and verify the robustness of the proposed PG-BEMD technique

Optics EXPRESS

to the general number of fringes present in the fringe pattern as in experimental conditions it can significantly vary. It is therefore highly desirable to design a versatile enhancement technique and be able to apply it to a broad range of experimental scenarios. Figure 10 presents the outcome of the numerical investigation. We compare the PG-BEMD with the MO-BEMD method. For the all studied number of fringes the PG-BEMD performs better. Especially for the higher number of fringes the quality of the fringe pattern decomposition provided by the proposed PG-BEMD is constantly and significantly better than the reference MO-BEMD, which suffers from the erroneous fringe skeletonizing. Starting from 50 carrier fringes per image the PG-BEMD outclasses its predecessor by a great margin due to the robust novel adaptive strategy. The analysis was made without the noise nor the denoising, as the BM3D is used in both models. We decided to assume ideal denoising capability at this point to highlight algorithm related feature.

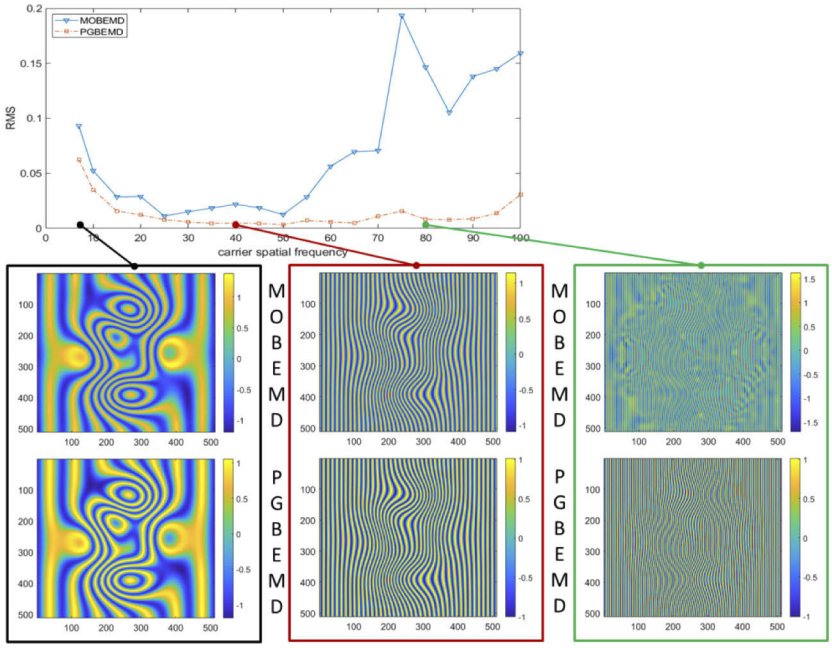

Fig. 10. The MO-BEMD and PG-BEMD decomposition comparison under varying carrier spatial frequency conditions.

3.3. *Fringe pattern feature investigation – background level (contrast loss)*

Using the previously described Matlab codes and altering the following formulas:

```
phase=x.^3/5 - 11*x - 2*y.^2+10*y+6*peaks(512);
```

```
gauss=C*normpdf(x.^2+y.^2,0,3); Im=3+cos(phase)+gauss;
```

we simulated a set of fringe patterns with the defined phase function and varying magnitude (C) of the background term defined by the Gaussian function. Strong background term influences the visibility of the fringes (contrast) hence it can both simulate the effect of the strong out of focus incoherent light component and low temporal-spatial coherence of the light source. The objective of this study is to test and verify the robustness of the proposed PG-BEMD technique to the general level of the background component (fringe visibility). As the background depends on a set of experimental conditions (coherence, polarization, reflectivity, transmission etc.) it is

Optics EXPRESS

desirable to derive a fringe enhancement method robust to background term variation and be able to apply it under challenging experimental conditions. Figure 11 presents the outcome of the simulation-driven investigation. We compare the PG-BEMD with the MO-BEMD method. It can be readily observed that for the background component magnitude C up to 15 the proposed PG-BEMD provides better background filtering. Further increasing the background level causes deterioration of the PG-BEMD adaptive envelope estimation and therefore hinders the final filtering result. It should be noted that the cut-off background magnitude around 15 is already a very significant value corresponding to the strong background. It should be rather easily controlled experimentally to stay under this level. The MO-BEMD background elimination is stable over wide range of background levels. Further stabilizing the PG-BEMD results is our goal for future studies.

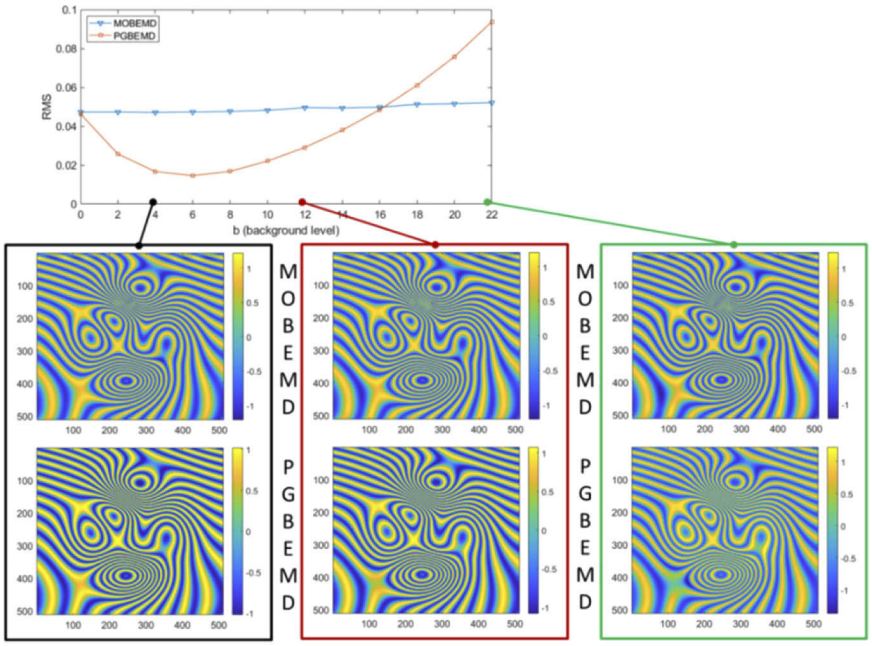

Fig. 11. The MO-BEMD and PG-BEMD comparison: varying background level case.

4. Experimental validation

We consider two cases for the experimental validation of the proposed PG-BEMD algorithm in comparison with the MO-BEMD approach. First experimental investigation concerned droplet evaporation examination using the digital holographic microscopy (DHM) technique [72,73]. Exemplifying hologram is presented in Fig. 12(a), whereas Figs. 12(b-c) show first two modes calculated using the PG-BEMD, and Figs. 12(d-e) depict first two modes obtained via the MO-BEMD technique. Complete condensed fringe term extracted by the PG-BEMD in its first mode is worth highlighting. The MO-BEMD outcomes exhibit strong mode-mixing effect due to substantial fringe period variation (note sparse fringes in the second mode).

Second experimental example comprises phase imaging of HeLa cells for bio-sensing applicability verification. Interference microscopy setup realizing the quantitative phase imaging [74,75] was employed. Interferogram containing fringes of varying period is presented in Fig. 13(a). Transparent live HeLa cells are to be visualized using the quantitative phase contrast [61–63] technique facilitated by the interferogram's phase map demodulation using Hilbert spiral

Optics EXPRESS

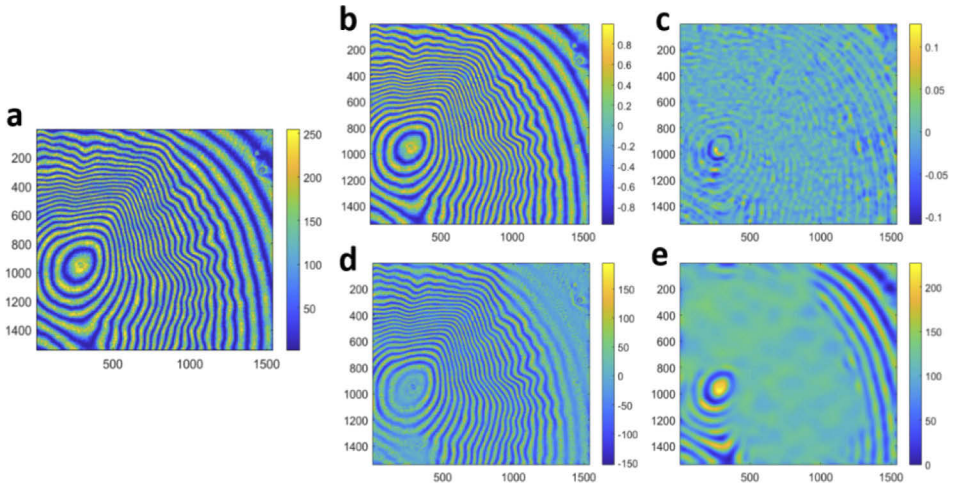

Fig. 12. Evaporating droplet study using DHM: (a) original hologram, 1st mode by (b) the PG-BEMD and (d) the MO-BEMD, 2nd mode by (c) the PG-BEMD and (e) the MO-BEMD.

transform [18]. It needs the background-filtered interferogram as input, hence the MO-BEMD and the PG-BEMD preprocessing is needed and performed, see Fig. 13(b) and Fig. 13(d), respectively. Interferogram noise was reduced using BM3D with sigma 10 in PG-BEMD case, whereas MO-BEMD was executed using the default settings [58]. Phase maps calculated using the HST suggest that the MO-BEMD, Fig. 13(c), upon erroneous decomposition induced phase errors (phase discontinuities mainly), whereas the PG-BEMD technique, Fig. 13(e), supplied high-quality pre-filtered data for the phase reconstruction.

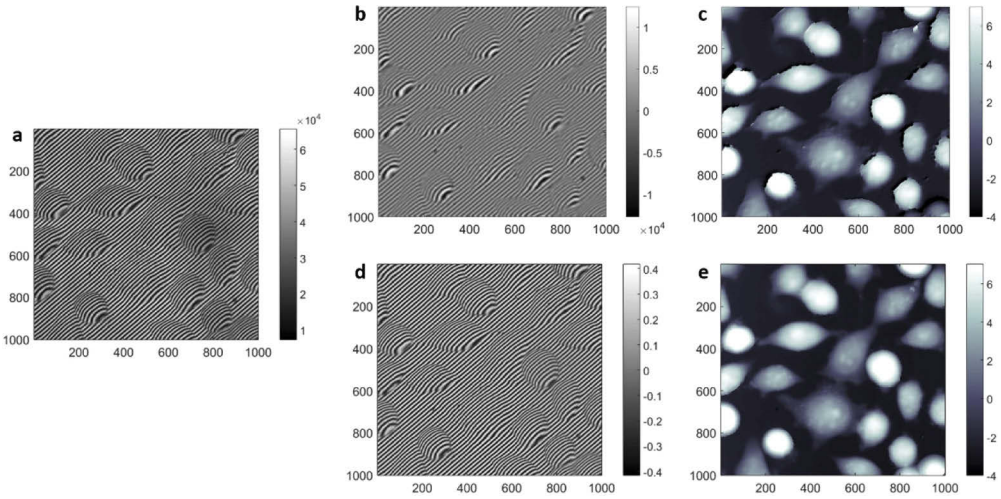

Fig. 13. HeLa cells study: (a) original interferogram, (b) interferogram pre-filtered using the MO-BEMD and (d) PG-BEMD methods, phase reconstructions (in radians) calculated using the Hilbert spiral transform based on (c) MO-BEMD and (e) PG-BEMD filtering results.

For quantitative evaluation we calculated the standard deviation (STD) and variance (VAR) of the gradients of the phase maps, Figs 13(c) and 13(e). Differentiation sensitizes quantitative evaluation to phase discontinuities. The MO-BEMD reached STD = 2,26 and VAR = 5,10, while

Optics EXPRESS

the PG-BEMD was able to decrease these values to STD = 0,22 and VAR = 0,05. It corroborates the proposed PG-BEMD for phase demodulation enhancement.

5. Closing remarks

Fringe pattern enhancement, i.e., the noise minimization and the background term removal, at the pre-processing stage prior to the phase map calculation is essential to minimize the jeopardizing effect of the intensity error sources. We proposed an automatic, robust and highly adaptive fringe pattern enhancement method based on the novel period-guided bidimensional empirical mode decomposition algorithm (PG-BEMD). The spatial distribution of the fringe period is estimated using the novel windowed approach and then serves as an indicator for the truly adaptive decomposition with the filter size locally adjusted to the fringe pattern density. In this way the fringe term can be successfully extracted in a single (first) component of the decomposition alleviating the cumbersome mode mixing phenomenon and greatly simplifying the signal reconstruction (no need for modes selection nor summation). Interferogram noise minimization is ensured employing the block matching 3D filtering of the intensity pattern prior to its decomposition. Comprehensive numerical studies corroborated superiority of the proposed approach over the regular EFEMD in terms of the automation, mode-mixing alleviation and quality of the reconstruction. The PG-BEMD was also numerically and experimentally positively-verified against the MO-BEMD sparse decomposition technique. Favorable influence of the PG-BEMD pre-filtering (in comparison with the MO-BEMD one) on the single-shot Hilbert spiral transform based phase demodulation was showcased in the HeLa cells QPI study. Presented results highlight a wide spreading range of possible application of the presented technique for the efficient and automatic enhancement of diverse interferograms/holograms – a crucial step in the emerging QPI techniques and well-established interferometric methods.

For the 1000×1000 px image presented in Fig. 13(a) the MO-BEMD algorithm (with default settings on) needs around 48 seconds to complete computations, whereas the PG-BEMD executes in around 25 seconds, including BM3D filtering (CPU 2.6 GHz, 16 GB RAM, Matlab 2019a). Computation time scales with image size, and for exemplifying 500×500 pixel image (1/4 of the Fig. 13(a)) reads 19 s and 13 s for the MO-BEMD and PG-BEMD, respectively. The BM3D is responsible for the majority of the processing time of PG-BEMD in this case (around 9 s for sigma 10). It is worth emphasizing that although the fringe period estimation itself is rather time consuming, the novel empirical decomposition it guides is completed by extracting only the first BIMF, in a single iteration of the sifting process. The MO-BEMD needs significantly more iterations (precisely 7 in the case presented in Fig. 13), especially for dense fringes, which is the main computational burden. On the other hand, the EFEMD technique could have much longer computation times mainly due to large number of extracted BIMFs. We will seek the further acceleration of the PG-BEMD in the future works.

Funding

Narodowe Centrum Nauki (2017/25/B/ST7/02049); National Agency for Academic Exchange (PPN/BEK/2018/1/00511); Ministerio de Economía y Competitividad (FIS2017-89748-P); Politechnika Warszawska (Statutory funds).

Acknowledgments

This work has been supported by the Warsaw University of Technology statutory funds (Faculty of Mechatronics Dean's Grant and Institute of Micromechanics and Photonics subvention).

Disclosures

The authors declare no conflicts of interest.

Optics EXPRESS

References

1. J. Schwider, "Advanced evaluation techniques in interferometry," in *Prog. Opt.*, E. Wolf, ed. (Elsevier, 1990).
2. D. W. Robinson and G. Reid, *Interferogram Analysis: Digital Fringe Pattern Measurement* (Institute of Physics Publishing, 1993).
3. D. Malacara ed., *Optical Shop Testing* (Jon Wiley and Sons, 2007).
4. M. Servin, J. A. Quiroga, and M. Padilla, *Fringe Pattern Analysis for Optical Metrology: Theory, Algorithms, and Applications* (Wiley, 2014).
5. M. Takeda, H. Ina, and S. Kobayashi, "Fourier-transform method of fringe-pattern analysis for computer-based topography and interferometry," J. Opt. Soc. Am. **72**(1), 156–160 (1982).
6. Q. Kemao, "Windowed Fourier transform for fringe pattern analysis," Appl. Opt. **43**(13), 2695–2702 (2004).
7. Q. Kemao, *Windowed Fringe Pattern Analysis* (SPIE, 2013).
8. L. R. Watkins, S. M. Tan, and T. H. Barnes, "Determination of interferometer phase distributions by use of wavelets," Opt. Lett. **24**(13), 905–907 (1999).
9. Z. Wang and H. Ma, "Advanced continuous wavelet transform algorithm for digital interferogram analysis and processing," Opt. Eng. **45**(4), 045601 (2006).
10. K. Pokorski and K. Patorski, "Visualization of additive-type moiré and time-average fringe patterns using the continuous wavelet transform," Appl. Opt. **49**(19), 3640–3651 (2010).
11. K. Patorski and K. Pokorski, "Examination of singular scalar light fields using wavelet processing of fork fringes," Appl. Opt. **50**(5), 773–781 (2011).
12. L. Kai and Q. Kemao, "Improved generalized regularized phase tracker for demodulation of a single fringe pattern," Opt. Express **21**(20), 24385–24397 (2013).
13. M. Servin, J. L. Marroquin, and F. J. Cuevas, "Demodulation of a single interferogram by use of a two-dimensional regularized phase-tracking technique," Appl. Opt. **36**(19), 4540–4548 (1997).
14. M. Servin, J. L. Marroquin, and F. J. Cuevas, "Fringe follower regularized phase tracker for demodulation of closed-fringe interferograms," J. Opt. Soc. Am. A **18**(3), 689–695 (2001).
15. C. Tian, Y. Yang, D. Liu, Y. Luo, and Y. Zhuo, "Demodulation of a single complex fringe interferogram with a path-independent regularized phase-tracking technique," Appl. Opt. **49**(2), 170–179 (2010).
16. M. Kujawinska and J. Wojciak, "Spatial-carrier phase-shifting technique of fringe pattern analysis," Proc. SPIE **1508**, 61–67 (1991).
17. M. Pirga and M. Kujawinska, "Two directional spatial-carrier phase-shifting method for analysis of crossed and closed fringe patterns," Opt. Eng. **34**(8), 2459–2466 (1995).
18. Y. Du, G. Feng, H. Li, J. Vargas, and S. Zhou, "Spatial carrier phase-shifting algorithm based on principal component analysis method," Opt. Express **20**(15), 16471–16479 (2012).
19. K. G. Larkin, D. J. Bone, and M. A. Oldfield, "Natural demodulation of two-dimensional fringe patterns. I. General background of the spiral phase quadrature transform," J. Opt. Soc. Am. A **18**(8), 1862–1870 (2001).
20. J. A. Guerrero, J. L. Marroquin, M. Rivera, and J. A. Quiroga, "Adaptive monogenic filtering and normalization of ESPI fringe patterns," Opt. Lett. **30**(22), 3018–3020 (2005).
21. M. Wielgus, K. Patorski, P. Etchepareborda, and A. Federico, "Continuous phase estimation from noisy fringe patterns based on the implicit smoothing splines," Opt. Express **22**(9), 10775–10791 (2014).
22. R. Kulkarni and P. Rastogi, "Phase derivative estimation from a single interferogram using a Kalman smoothing algorithm," Opt. Lett. **40**(16), 3794–3797 (2015).
23. R. Kulkarni and P. Rastogi, "Simultaneous measurement of in-plane and out-of-plane displacements using pseudo-Wigner-Hough transform," Opt. Express **22**(7), 8703–8711 (2014).
24. R. Kulkarni and P. Rastogi, "Iterative signal separation based multiple phase estimation in digital holographic interferometry," Opt. Express **23**(20), 26842–26852 (2015).
25. J. A. Quiroga, J. A. Gómez-Pedrero, and Á García-Botella, "Algorithm for fringe pattern normalization," Opt. Commun. **197**(1-3), 43–51 (2001).
26. J. A. Quiroga and M. Servin, "Isotropic n-dimensional fringe pattern normalization," Opt. Commun. **224**(4-6), 221–227 (2003).
27. H. Zou, X. Zhou, H. Zhao, T. Yang, H. Du, F. Gu, and Z. Zhao, "Color fringe-projected technique for measuring dynamic objects based on bidimensional empirical mode decomposition," Appl. Opt. **51**(16), 3622–3630 (2012).
28. S. Li, X. Su, W. Chen, and L. Xiang, "Eliminating the zero spectrum in Fourier transform profilometry using empirical mode decomposition," J. Opt. Soc. Am. A **26**(5), 1195–1201 (2009).
29. C. Wang and F. Da, "Phase demodulation using adaptive windowed Fourier transform based on Hilbert-Huang transform," Opt. Express **20**(16), 18459–18477 (2012).
30. Y. Xue, J. Cao, R. Tian, H. Du, and Y. Shu, "Application of the empirical mode decomposition and wavelet transform to seismic reflection frequency attenuation analysis," J. Pet. Sci. Eng. **122**, 360–370 (2014).
31. N. E. Huang, Z. Shen, S. R. Long, M. C. Wu, H. H. Shih, Q. Zheng, N.-C. Yen, C. C. Tung, and H. H. Liu, "The empirical mode decomposition and the Hilbert spectrum for non-linear and non-stationary time series analysis," Proc. R. Soc. London, Ser. A **454**(1971), 903–995 (1998).
32. C. Damerval, S. Meignen, and V. Perrier, "A fast algorithm for bidimensional EMD," IEEE Signal Process. Lett. **12**(10), 701–704 (2005).

Optics EXPRESS

33. J. C. Nunes, Y. Bouaoune, E. Delechelle, O. Niang, and P. Bunel, "Image analysis by bidimensional empirical mode decomposition," Image Vis. Comput. **21**(12), 1019–1026 (2003).
34. S. M. A. Bhuiyan, N. O. Attoh-Okine, K. E. Barner, A. Y. Ayenu-Prah, and R. R. Adhami, "Bidimensional empirical mode decomposition using various interpolation techniques," Adv. Adapt. Data Anal. **01**(02), 309–338 (2009).
35. M. B. Bernini, A. Federico, and G. H. Kaufmann, "Noise reduction in digital speckle pattern interferometry using bidimensional empirical mode decomposition," Appl. Opt. **47**(14), 2592–2598 (2008).
36. M. Wielgus and K. Patorski, "Denoising and extracting background from fringe patterns using midpoint-based bidimensional empirical mode decomposition," Appl. Opt. **53**(10), B215–B222 (2014).
37. M. B. Bernini, A. Federico, and G. H. Kaufmann, "Normalization of fringe patterns using the bidimensional empirical mode decomposition and the Hilbert transform," Appl. Opt. **48**(36), 6862–6869 (2009).
38. M. B. Bernini, A. Federico, and G. H. Kaufmann, "Phase measurement in temporal speckle pattern interferometry signals presenting low-modulated regions by means of the bidimensional empirical mode decomposition," Appl. Opt. **50**(5), 641–647 (2011).
39. M. Wielgus and K. Patorski, "Evaluation of amplitude encoded fringe patterns using the bidimensional empirical mode decomposition and the 2D Hilbert transform generalizations," Appl. Opt. **50**(28), 5513–5523 (2011).
40. X. Zhou, H. Zhao, and T. Jiang, "Adaptive analysis of optical fringe patterns using ensemble empirical mode decomposition algorithm," Opt. Lett. **34**(13), 2033–2035 (2009).
41. Y. Zhou and H. Li, "Adaptive noise reduction method for DSPI fringes based on bi-dimensional ensemble empirical mode decomposition," Opt. Express **19**(19), 18207–18215 (2011).
42. S. M. A. Bhuiyan, R. R. Adhami, and J. F. Khan, "Fast and adaptive bidimensional empirical mode decomposition using order-statistics filter based envelope estimation," EURASIP J. Adv. Signal Process. **2008**(1), 728356 (2008).
43. M. Trusiak, K. Patorski, and M. Wielgus, "Adaptive enhancement of optical fringe patterns by selective reconstruction using FABEMD algorithm and Hilbert spiral transform," Opt. Express **20**(21), 23463–23479 (2012).
44. K. Patorski, K. Pokorski, and M. Trusiak, "Fourier domain interpretation of real and pseudo-moiré phenomena," Opt. Express **19**(27), 26065–26078 (2011).
45. M. Trusiak and K. Patorski, "Space domain interpretation of incoherent moiré superimpositions using FABEMD," Proc. SPIE **8697**, 869704 (2012).
46. M. Trusiak, K. Patorski, and K. Pokorski, "Hilbert-Huang processing for single-exposure two-dimensional grating interferometry," Opt. Express **21**(23), 28359–28379 (2013).
47. M. Wielgus, A. Antoniewicz, M. Bartyś, and B. Putz, "Fast and adaptive bidimensional empirical mode decomposition for the real-time video fusion," *Proc. FUSION* 6289864, 649–654 (2012).
48. M. Trusiak, M. Wielgus, and K. Patorski, "Advanced processing of optical fringe patterns by automated selective reconstruction and enhanced fast empirical mode decomposition," Opt. Lasers Eng. **52**(1), 230–240 (2014).
49. M. Trusiak, K. Patorski, and M. Wielgus, "Hilbert-Huang processing and analysis of complex fringe patterns," Proc. SPIE **9203**, 92030K (2014).
50. M. Trusiak, Ł Służewski, and K. Patorski, "Single shot fringe pattern phase demodulation using Hilbert-Huang transform aided by the principal component analysis," Opt. Express **24**(4), 4221–4238 (2016).
51. M. Trusiak and K. Patorski, "Two-shot fringe pattern phase-amplitude demodulation using Gram-Schmidt orthonormalization with Hilbert-Huang pre-filtering," Opt. Express **23**(4), 4672–4690 (2015).
52. M. Wielgus, Z. Sunderland, and K. Patorski, "Two-frame tilt-shift error estimation and phase demodulation algorithm," Opt. Lett. **40**(15), 3460–3463 (2015).
53. Z. Sunderland, K. Patorski, and M. Trusiak, "Subtractive two-frame three-beam phase-stepping interferometry for testing surface shape of quasi-parallel plates," Opt. Express **24**(26), 30505–30513 (2016).
54. K. Patorski, M. Trusiak, and T. Tkaczyk, "Optically-sectioned two-shot structured illumination microscopy with Hilbert-Huang processing," Opt. Express **22**(8), 9517–9527 (2014).
55. M. Trusiak, V. Mico, J. Garcia, and K. Patorski, "Quantitative phase imaging by single-shot Hilbert–Huang phase microscopy," Opt. Lett. **41**(18), 4344–4347 (2016).
56. JÁ Picazo-Bueno, M. Trusiak, J. García, K. Patorski, and V. Micó, "Hilbert–Huang single-shot spatially multiplexed interferometric microscopy," Opt. Lett. **43**(5), 1007–1010 (2018).
57. C. Wang, Q. Kemao, and F. Da, "Automatic fringe enhancement with novel bidimensional sinusoids-assisted empirical mode decomposition," Opt. Express **25**(20), 24299–24311 (2017).
58. X. Zhou, A. G. Podoleanu, Z. Yang, T. Yang, and H. Zhao, "Morphological operation-based bi-dimensional empirical mode decomposition for automatic background removal of fringe patterns," Opt. Express **20**(22), 24247–24262 (2012).
59. X. Zhu, Z. Chen, and C. Tang, "Variational image decomposition for automatic background and noise removal of fringe patterns," Opt. Lett. **38**(3), 275–277 (2013).
60. M. Cywińska, M. Trusiak, and K. Patorski, "Automatized fringe pattern preprocessing using unsupervised variational image decomposition," Opt. Express **27**(16), 22542–22562 (2019).
61. Y. Park, C. Depeursinge, and G. Popescu, "Quantitative phase imaging in biomedicine," Nat. Photonics **12**(10), 578–589 (2018).
62. G. Popescu, *Quantitative Phase Imaging of Cells and Tissues* (McGraw-Hill, 2011).
63. N. T. Shaked, Z. Zalevsky, and L. L. Satterwhite, *Biomedical Optical Phase Microscopy and Nanoscopy* (Academic Press, 2012).

Optics EXPRESS

64. H. Wang and Q. Kemao, "Boundary-aware single fringe pattern demodulation," Opt. Express **25**(26), 32669–32685 (2017).
65. H. Guo, Q. Yang, and M. Chen, "Local frequency estimation for the fringe pattern with a spatial carrier: principle and applications," Appl. Opt. **46**(7), 1057–1065 (2007).
66. K. Li and B. Pan, "Frequency-guided windowed Fourier ridges technique for automatic demodulation of a single closed fringe pattern," Appl. Opt. **49**(1), 56–60 (2010).
67. Q. Kemao and S. H. Soon, "Sequential demodulation of a single fringe pattern guided by local frequencies," Opt. Lett. **32**(2), 127–129 (2007).
68. L. Kai and Q. Kemao, "Fast frequency-guided sequential demodulation of a single fringe pattern," Opt. Lett. **35**(22), 3718–3720 (2010).
69. H. Wang and Q. Kemao, "Frequency guided methods for demodulation of a single fringe pattern," Opt. Express **17**(17), 15118–15127 (2009).
70. K. Dabov, A. Foi, V. Katkovnik, and K. Egiazarian, "Image denoising by sparse 3-D transform-domain collaborative filtering," IEEE Trans. on Image Process. **16**(8), 2080–2095 (2007).
71. P. Zdankowski, M. Trusiak, D. McGloin, and J. R. Swedlow, "Numerically enhanced adaptive optics-based 3D STED microscopy for deep-tissue super-resolved imaging," ACS Nano. **14**(1), 394–405 (2020).
72. Y. Tsoumpas, S. Dehaeck, A. Rednikov, and P. Colinet, "Effect of Marangoni Flows on the Shape of Thin Sessile Droplets Evaporating into Air," Langmuir **31**(49), 13334–13340 (2015).
73. S. Dehaeck, Y. Tsoumpas, and P. Colinet, "Analyzing closed-fringe images using two-dimensional Fan wavelets," Appl. Opt. **54**(10), 2939–2952 (2015).
74. A. Ahmad, V. Dubey, G. Singh, V. Singh, and D. S. Mehta, "Quantitative phase imaging of biological cells using spatially low and temporally high coherent light source," Opt. Lett. **41**(7), 1554–1557 (2016).
75. V. Dubey, G. Singh, V. Singh, A. Ahmad, and D. S. Mehta, "Multispectral quantitative phase imaging of human red blood cells using inexpensive narrowband multicolor LEDs," Appl. Opt. **55**(10), 2521–2525 (2016).